

Andreas Macrander · Rolf H. Käse · Uwe Send ·  
Héðinn Valdimarsson · Steingrímur Jónsson

## Spatial and temporal structure of the Denmark Strait Overflow revealed by acoustic observations

Received: 4 January 2006 / Accepted: 21 December 2006 / Published online: 24 February 2007  
© Springer-Verlag 2007

**Abstract** In spite of the fundamental role the Atlantic Meridional Overturning Circulation (AMOC) plays for global climate stability, no direct current measurement of the Denmark Strait Overflow, which is the densest part

of the AMOC, has been available until recently that resolve the cross-stream structure at the sill for long periods. Since 1999, an array of bottom-mounted acoustic instruments measuring current velocity and bottom-to-surface acoustic travel times was deployed at the sill. Here, the optimization of the array configuration based on a numerical overflow model is discussed. The simulation proves that more than 80% of the dense water transport variability is captured by two to three acoustic current profilers (ADCPs). The results are compared with time series from ADCPs and Inverted Echo Sounders deployed from 1999 to 2003, confirming that the dense overflow plume can be reliably measured by bottom-mounted instruments and that the overflow is largely geostrophically balanced at the sill.

Responsible editor: Stephen R. Rintoul

A. Macrander (✉)  
Alfred-Wegener-Institut für Polar- und Meeresforschung,  
Büsestr. 24,  
27570 Bremerhaven, Germany  
e-mail: Andreas.Macrander@awi.de  
Tel.: +49-471-48311881  
Fax: +49-471-48311797

A. Macrander · R. H. Käse  
IFM-GEOGRAPHY, Kiel, Germany

R. H. Käse  
Institut für Meereskunde,  
Bundesstr. 53,  
20146 Hamburg, Germany  
e-mail: kaese@ifm.uni-hamburg.de

U. Send  
Scripps Institution of Oceanography,  
University of California,  
Mail Code 0230,  
San Diego, La Jolla, CA 92093-0230, USA  
e-mail: usend@ucsd.edu

H. Valdimarsson  
Marine Research Institute,  
Skúlagata 4,  
121 Reykjavík, Iceland  
e-mail: hv@hafro.is

S. Jónsson  
University of Akureyri,  
Borgir v/Norðurslóð,  
600 Akureyri, Iceland  
e-mail: steing@unak.is

S. Jónsson  
MRI, Reykjavík, Iceland

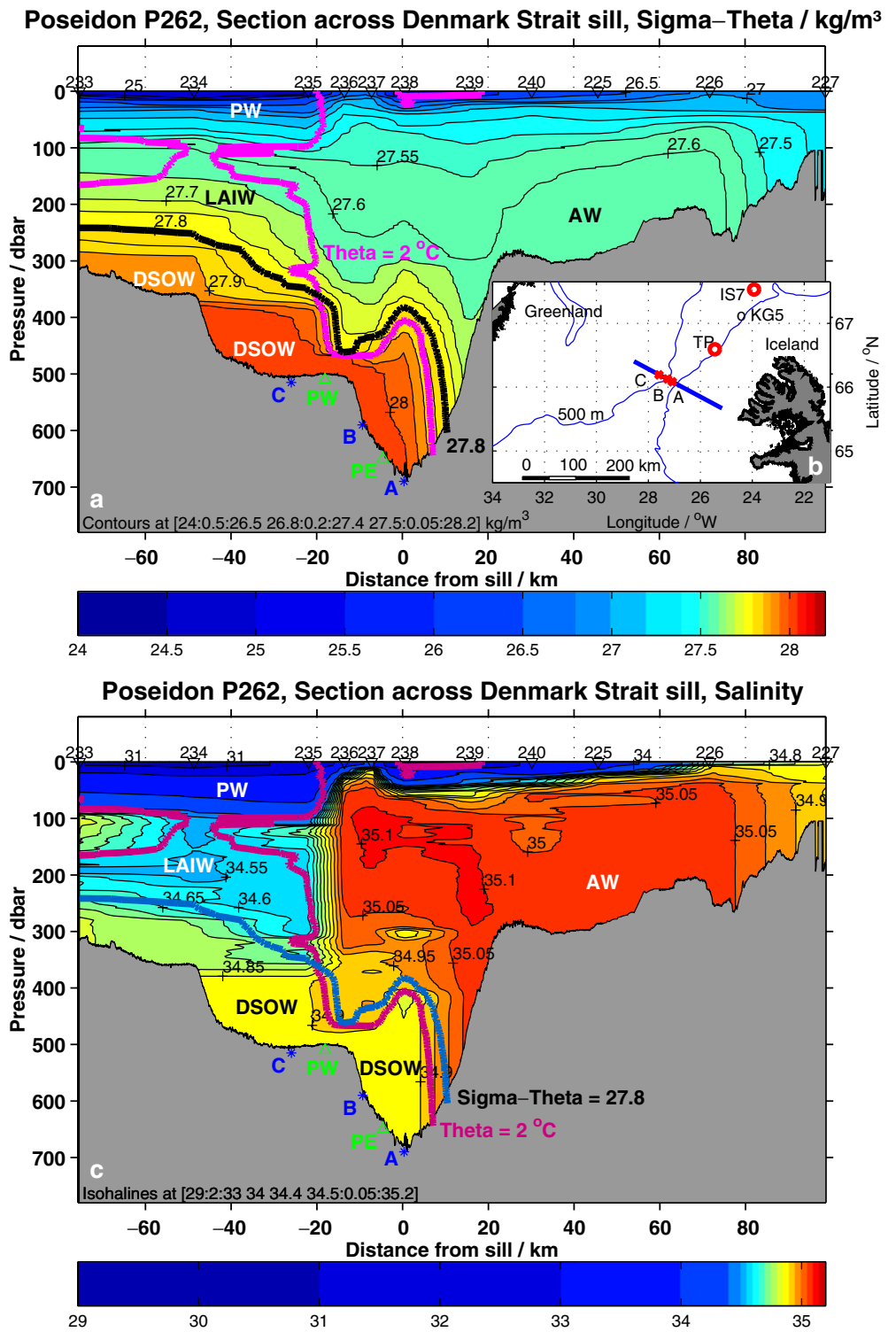
**Keywords** Denmark Strait Overflow · Acoustic observations · ADCP · PIES · Geostrophy

### 1 Introduction

The Atlantic Meridional Overturning Circulation (AMOC) is an important part of the global heat budget, transferring warm surface waters northward to high latitudes. There, they are transformed to cold dense deep waters, eventually returning as North Atlantic Deep Water (NADW). A large part of the NADW is formed in the Nordic Seas, entering the deep ocean as overflows across the Greenland–Scotland Ridge (Hansen and Østerhus 2000). The densest NADW component is the Denmark Strait Overflow Water (DSOW), which is formed from various sources in the Nordic Seas (Rudels et al. 2002; Mauritzen 1996). This project studies the Denmark Strait Overflow (DSO) on a section across the sill between Iceland and Greenland (Fig. 1).

During the past three decades, several short term studies were carried out in the Denmark Strait (maximum duration of 1 year), but no longer continuous time series exist that resolve the complicated cross-stream structure of the overflow at the sill. Since Worthington (1969), Agaard and Malmberg (1978), and Ross (1984), the DSO was regarded as a feature highly variable on time scales of a few days, but

**Fig. 1** **a** Potential density section across the Denmark Strait sill (“Poseidon” cruise P262, August 2000). **b** Map of Denmark Strait: 500 m isobath marked as black line, the heavy blue line denotes the location of the hydrographic section. *A*, *B*, and *C* mark positions of moored ADCPs, *TP* denotes a temperature sensor mooring in the upstream region. *IS7* marks the position of an Icelandic current meter mooring (Jónsson 1999), *KG5* the repeated hydrographic station Kögur 5. **c** Salinity, same section as **a**. In both sections, Inverted Echo Sounders are marked as *PE* and *PW*, respectively; *A*, *B* and *C* indicate moored ADCPs. Note the nonlinear color scale. The  $\sigma_{\Theta} = 27.8 \text{ kg/m}^3$  isopycnal and, additionally, the  $\Theta = 2.0^\circ\text{C}$  isotherm are highlighted. For abbreviations of water masses, see text



with no significant seasonal or interannual variability (Aagaard and Malmberg 1978; Dickson and Brown 1994). At the sill, DSOW transports have been estimated to be 2.9 (Ross 1984; Girton et al. 2001) or 2.5 Sv (Saunders 2001). Recently, possible links of NADW variability to the North Atlantic Oscillation (NAO) or changes in deep water formation in the Nordic Seas are discussed (Dickson et al. 1996, 1999; McCartney et al. 1998; Bacon 1998; Biastoch et

al. 2003). Macrander et al. (2005) observed a 20% transport decrease from 1999 to 2003, which might be related to a decreasing NAO and dense water reservoir height. This view is supported by a recent model study of Käse (2006).

The long term goal of this study carried out at Kiel University Sonderforschungsbereich (SFB) 460, Institut für Meereskunde Hamburg, and the Marine Research Institute Reykjavík is to quantify the overflow during a

longer period than before and with cross-strait resolution to observe possible long-term variability and its sensitivity to climate change (Macrander et al. 2005).

As a basis for these observations, the principal technique to measure the dense overflow transport by means of moored acoustic Doppler current profilers (ADCP) and pressure sensor-equipped inverted echo sounders (PIES) is investigated in this paper.

First, the dominant hydrographic features of the Denmark Strait are discussed. Different acoustic interface detection techniques are compared proving the feasibility of plume thickness measurements based on bottom-mounted ADCP and PIES.

Second, the acoustic measurements are simulated within a high-resolution model of the DSO to optimize number and positions of the moorings. The chosen configuration is an optimized compromise between full cross-strait coverage, resolution of overflow eddy scales, and available technical resources. Systematic transport estimate biases caused by the chosen sampling geometry of the mooring array are quantified.

In the following, the actual observations from 1999 to 2003 are discussed. While the interannual variability has been addressed by Macrander et al. (2005), plume dynamics and geostrophy on shorter time scales are investigated here.

## 2 Hydrographic background

Sea straits as key regions of the ocean circulation are often chosen for transport measurements because they focus the flows through choke points and, in the case of marginal seas, also allow estimates of integral budgets within the enclosed seas. The Denmark Strait between Greenland and Iceland (Fig. 1) is a major gateway of the Greenland–Scotland ridge, linking Nordic Seas and the open North Atlantic. The DSO represents the densest part of the AMOC (Saunders 2001).

The sill is roughly 630 m deep (Jónsson and Valdimarsson 2004a,b). Dense overflow water occupies an approximately 100-km-wide part of the strait where it is deeper than 300 m. Because the internal Rossby radius is around 14 km, the Denmark Strait may be considered as “wide strait” (Whitehead 1998), which has consequences for the structure of the throughflow (Gill 1977; Killworth and McDonald 1993; Borenäs and Lundberg 1986; Nikolopoulos et al. 2003, and others). A density section at the sill (Fig. 1a) shows DSOW characterized by water denser than  $\sigma_\Theta = 27.8 \text{ kg/m}^3$  and a typical maximum density larger than  $\sigma_\Theta = 28.0 \text{ kg/m}^3$ . This water mass is stretched along the Greenland side of the continental slope. Although not obvious in the density section, the lighter water above the DSOW consists of two different water masses clearly separated by temperature and salinity fronts (Fig. 1b): Warm, saline Atlantic water (AW) on the Iceland side of the strait with densities near 27.6 and cold, fresher water of polar origin (Polar water, PW, and Lower Arctic Intermediate Water, LAIW) on the Greenland side (Swift 1986; Rudels et al. 2002). The dominant density

contrast of 0.3 to  $0.45 \text{ kg/m}^3$  (Whitehead 1998; Girton 2001), respectively between DSOW and AW/PW/LAIW, is the major driving force for the exchange flow through the strait.

The location of the fronts between the different water masses shows large variability, and thus, the hydrographic section displayed in Fig. 1 is just one typical realization. The overflow plume thickness at the sill typically varies between 50 and 400 m. The high spatial variability on the section requires more than one moored instrument to obtain accurate DSOW transport estimates.

## 3 Materials and methods

The Denmark Strait is a hostile environment for ships and moored equipment. In the East Greenland Current, access for research vessels is impeded by sea ice. Further, heavy fishing activities in parts of the ice-free zones pose serious risk on conventional taught-wire moorings. Hence, bottom-mounted acoustic instruments, which are shield protected against trawling hazards, are preferable.

In this study, the performance of bottom-mounted ADCP and PIES measuring the DSO plume thickness and transport is assessed. The acoustic observation methods are validated and optimized both in a numerical model and by comparison of different field measurements.

### 3.1 High-resolution DSO model

To optimize the observation strategy, the Käse and Oschlies (2000) Denmark Strait Primitive Equation model is used here. The model domain covers a  $940 \times 580 \text{ km}^2$  area aligned along the axis of the strait, with a horizontal resolution of approximately 4.5 km and 31 bottom-following  $\sigma$ -levels.

The density contrast between DSOW and the overlying lighter water masses responsible for the exchange flow is realized by a linearized equation of state where density is entirely defined by temperature. This simplification is feasible because the temperature and salinity contrasts between the lighter water masses in the Denmark Strait have a compensating effect on density. Hence, the cold and fresh East Greenland Current and the warm and saline AW exhibit essentially similar densities (Fig. 1). The temperature and salinity contrasts are irrelevant for the realistic reproduction of the short-term dynamics of the overflow, which entirely depends on the density structure. Further, the model does not include atmospheric or other external forcing, which is not necessary to reproduce the short-term dynamics of the overflow (Käse et al. 2003).

For this study, the model experiment was initialized with dense water in the upstream basin below 150 m depth and light water elsewhere, representing both the East Greenland Current and the Irminger Current. After a “dambreak” at  $t = 0$ , an overflow plume descends into the downstream basin, driven by the density difference of  $0.48 \text{ kg/m}^3$ .

Rudels et al. (2002) attribute most of the overflow to components advected by the East Greenland Current. However, direct current meter measurements (Jónsson 1999; Jónsson and Valdimarsson 2004a,b) show persistent flow of water with DSOW properties along the Iceland shelf edge towards the sill originating from the Iceland Sea, consistent with the model results (Fig. 2). The stream function indicates that most of the flow crossing the sill originates from the Iceland Sea rather than the Greenland side of the upstream basin. At the sill, most of the DSOW transport is confined to the deep part of the strait; the Greenland shelf region further to the northwest contributes less than 1 Sv because of recirculations.

Previous modeling results indicated that dominant features of the overflow are well represented in numerical simulation when a realistic topography and an appropriate resolution are used (Girton 2001; Käse et al. 2003). This suggests that the model might be a suitable testbed to implement and optimize different measurement strategies.

### 3.2 Observation methods with acoustic instruments and optimization in the model

Because at the sill, the mean flow is confined to a narrow band (Fig. 1), it is tempting to rely on just one instrument

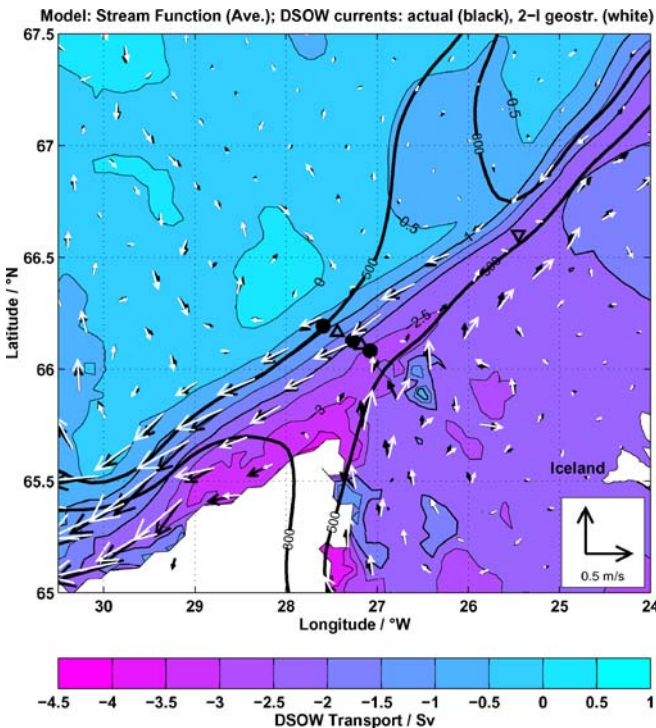


**Fig. 2** Model: time averaged dense water transport streamfunction (shaded contours). The bulk of the transport approaches the sill from the Iceland side; downstream, the overflow descends along the Greenland shelf edge. Note that the actual average dense water velocity (black vectors) almost equals lower layer velocity calculated from two-layer geostrophy (white vectors). The current acceleration downstream of the sill reflects the thinning of the overflow layer. 500 and 800 m isobaths additionally marked as heavy lines

that measures the vertical velocity profile. Multiplied by a scale factor, the vertical integral would yield the total throughflow. However, such single-point observations may be biased by lateral shifts of the overflow. In the following, the performance of single- and multi-instrument arrays to quantify the absolute overflow transport is investigated.

Different instrumental techniques are simulated at arbitrary model grid points on a cross-sill section to determine the optimal location of instruments with a constraint for the total number of resources. Both integrating geostrophic and direct velocity measurements are discussed.

*Integrating geostrophic measurements* can be obtained with a PIES (Meinen and Watts 1998). It measures bottom-to-surface acoustic travel time and bottom pressure with high precision. Acoustic travel time varies with bottom-to-surface path length and sound velocity, which depends predominantly on temperature. The thermal structure in the DSO can be approximated by two layers with uniform temperature (Fig. 5).

With pressure as the vertical axis,  $T_1, S_1$  and  $T_2, S_2$  as upper and lower layer properties, respectively, acoustic travel time is defined by

$$t_{PIES} = 2 \int_{p_{PIES}}^{p_{int}} \frac{1}{g\varrho(S_2, T_2, p)} \frac{1}{C_s(S_2, T_2, p)} dp + 2 \int_{p_{int}}^0 \frac{1}{g\varrho(S_1, T_1, p)} \frac{1}{C_s(S_1, T_1, p)} dp \quad (1)$$

with pressure  $p_{int}$  at the interface depth, acceleration of gravity  $g$  and density  $\varrho$  and sound speed  $C_s$  as function of  $S$ ,  $T$ , and  $p$  (UNESCO International Equation of State IES80, see Fofonoff 1985).

The distance between PIES and sea surface (i.e., water depth minus height of the PIES itself)  $D_{PIES}$  is then given by

$$D_{PIES} = \int_{p_{PIES}}^{p_{int}} \frac{1}{g\varrho(S_2, T_2, p)} dp + \int_{p_{int}}^0 \frac{1}{g\varrho(S_1, T_1, p)} dp. \quad (2)$$

With known temperatures and salinities of both layers, the system of Eqs. 1 and 2 can be solved for the two unknowns  $D_{PIES}$  and AW/DSOW interface depth  $p_{int}$ . Anomalies of  $D_{PIES}$  represent vertical deviations of the sea surface height (SSH).

For  $T_2$ , the temperature measurements of the PIES were assumed to be representative. For the upper layer, no time series are available from a bottom mounted instrument; hence, a constant temperature  $T_1 = 8^\circ\text{C}$  was assumed, based on hydrographic data. Salinities, although minor

influence on sound speed, were determined by an empirical  $T/S$  relation also derived from hydrographic data. With these parameters set, Eqs. 1 and 2 are solved numerically to obtain the two unknowns  $D_{PIES}$  and interface depth  $p_{int}$ . Anomalies of  $D_{PIES}$  represent vertical deviations of the SSH. With the known  $T/S$  profile, the interface depth  $p_{int}$  can be derived from  $p_{int}$ .

A systematic study was carried out to test the effect of different choices for  $T_1$  and  $T_2$  (including temperatures closer to the mean layer temperatures of 0 and 6°C (Fig. 5) instead of taking bottom and surface temperature). However, PIES measurements of  $T_2$  and  $T_1 = 8^\circ\text{C}$  proved to provide the best agreement between PIES data, hydrographic profiles obtained during deployment and recovery, and overflow plume thickness variability derived from velocity shear profiles measured by an adjacent ADCP.

With the additional constraint that the flow parallel to the strait is geostrophically balanced, the current velocities of the upper ( $v_1$ ) and lower ( $v_2$ ) layer are given by the Margules equation (Dietrich et al. 1975). Replacing the partial derivatives by finite differences, as obtained from instruments at two distinct positions, the following expression holds:

Upper layer:

$$v_1 = \frac{g}{f} \frac{\Delta\zeta}{\Delta x} \quad (3)$$

Lower layer:

$$v_2 = \frac{\varrho_1}{\varrho_2} v_1 + \frac{\Delta z_{int}}{\Delta x} \frac{g}{f} \frac{\Delta\varrho}{\varrho_2} \quad (4)$$

with  $g$  as acceleration of gravity, Coriolis parameter  $f$ , and upper/lower layer densities  $\varrho_1, \varrho_2$ , respectively.  $\Delta\varrho = \varrho_2 - \varrho_1$  denotes the density difference between both layers. SSH  $\zeta$  and interface depth  $z_{int}$  is measured by, e.g., moored PIES.  $\Delta x$  denotes the distance between the two observing instruments and  $v$  the geostrophic velocity component perpendicular to the connecting line between both instruments.

Because the absolute height of the PIES relative to the geoid is unknown, the velocities have to be corrected by a constant offset, which may be obtained from independent current observations, e.g., vessel mounted ADCP sections taken during the deployment. In this study, the two PIES were located only 13 km apart from each other (a distance in the order of the Rossby radius); therefore, the geostrophic  $v_1$  velocity could be referenced to match the actual mean surface velocity measured by ADCP B located between both PIES (see Section 4.5).

The DSOW transport is obtained by vertical integration of  $v_2$  from bottom to interface  $z_{int}$  and horizontal integration over the distance  $\Delta x$  between the observation instruments.

For *direct absolute velocity observations*, an ADCP is the instrument of choice. In the Denmark Strait with water depths shallower than 650 m, a 75-kHz ADCP is capable to

scan the entire water column. Transport estimates  $Q$  can be calculated for an array with  $N$  instruments using multilinear interpolation, equivalent to

$$Q = \sum_{i=1}^N x_i \int_{-H}^{Z_{li}} v_i dZ \quad (5)$$

with water depth  $H$ , upper DSOW interface depth  $Z_{li}$ ,  $v_i$  as measured current velocity parallel to the strait,  $x_i$  as a horizontal scale width, and  $i$  as index for the  $N$  instruments. All  $x_i$  were determined using multilinear regression and were optimized with respect to minimum variance between the “measured”  $Q$  and the known total DSOW transport in the model.

The upper DSOW interface can be identified by a maximum of current shear or acoustic backscatter, as will be shown in Section 4.2.

As a first test, both ADCP and PIES are placed at all model grid points on a cross-section at the sill. The resulting mean dense water transport ( $T < 2^\circ\text{C}$ ) is compared to the model truth. For this full instrument coverage in the model, the overall root mean square (RMS) transport error is  $< 8\%$  for ADCPs and interface defined by maximum current shear criteria (Fig. 4, thin black lines). Because the depth of the maximum current shear (detected by ADCPs) does not always coincide with the 27.8 isopycnal, minor discrepancies remain. Errors of  $< 12\%$  because of ageostrophic short-term variability and bottom friction are found for geostrophic estimates from simulated PIES (not shown). The temporal variability is captured with a correlation between measured and true transport of 0.99 for ADCP and 0.95 for PIES. Hence, the simulations demonstrate that it is

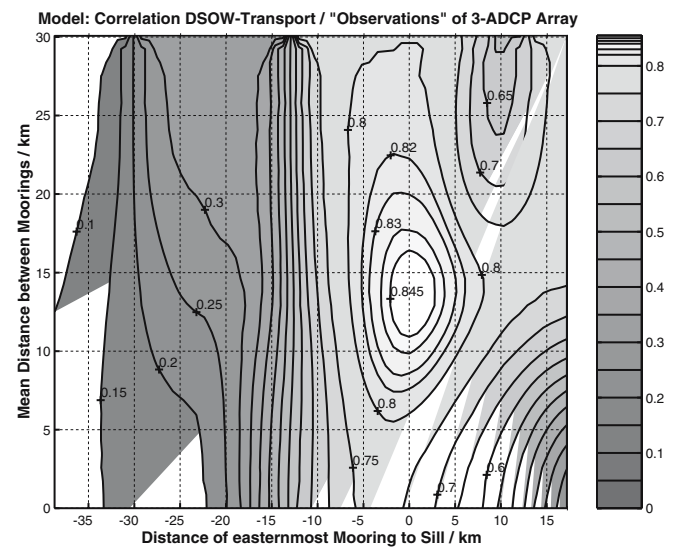


**Fig. 3** Optimization of the mooring array performance by simulation in the model. Shown is the correlation between “measured” and actual dense water transport in the model for three ADCP arrays. X-axis: Position of the easternmost mooring relative to the deepest part of the sill, Y-axis: Mean distance of the moorings to each other. All transports were calculated using multilinear regression; see text for details

**Table 1** Model results of multilinear regression between simulated ADCP observations and known total model DSOW transport

ADCP positions distance NW of sill	Deployed in field experiment	Scale widths $x_i$ (km)	Correlation $r$	Std. dev. $\sigma$ (Sv)	Mean dev. offset (Sv)
[0] [A]	1996–1999 + 2003–2005	22.6	0.50	1.49	1.23
[10] [ $\approx$ B]		26.1	0.69	1.22	0.71
[11 0] [B A]	1999–2001 + 2002–2003 + 2005–x	21.9 12.4	0.80	0.93	0.36
[25 11] [C B]	2001–2002	10.5 24.0	0.64	1.20	0.49
[25 11 0] [C B A]	2002 (May–Aug)	14.0 15.5 13.9	0.87	0.69	0.13
[45 27 13 2]		31.7 17.8 11.7 17.2	0.91	0.57	0.11

Characters A, B, C refer to ADCP positions indicated in Fig. 1. Scale widths refer to Eq. 5 used to calculate the overflow transport.

feasible to measure the dense overflow by means of bottom-mounted ADCPs and PIES.

Figure 3 depicts the correlation for a reduced measurement array of three ADCPs as a function of the distance of the easternmost mooring to the sill location ( $x$ -axis) and the mean distance between the instruments ( $y$ -axis). The contours show a clear correlation maximum of 0.87 at location (0, 14) km, representing the optimum configuration with the first instrument (“A”) deployed at the deepest part of the sill and the others (“B” and “C”) at the Greenland slope separated by roughly the Rossby-radius distance. Further investigations with nonequidistant spacing revealed that the optimum positions for a three-ADCP configuration are located 0 (A), 11 (B), and 25 km (C) northwest of the sill. For arrays with 1, 2, 3, and 4 instruments, the best results are listed in Table 1.

With a single instrument, a maximum correlation of just  $\leq 0.69$  between the “measured” and true transport is achieved; unresolved spatial fluctuations result in large RMS errors<sup>1</sup> of at least  $\sigma = 1.22$  Sv (Fig. 4, top panels). From 1996 to 1999 and 2003 to 2005, a single ADCP was deployed at A in the framework of the Variability of Exchanges in the Northern Seas (VEINS)/Arctic/Subarctic Ocean Fluxes West (ASOF-W) projects. For this location, the model simulation indicates a correlation level of  $r = 0.50$ .

A second device raises the correlation level to  $r = 0.80$ , but still,  $\sigma = 0.93$  Sv is caused by the flow across the Greenland shelf not covered by the array. The optimized three-ADCP array ( $r = 0.87$ ,  $\sigma = 0.69$  Sv) was implemented in the field experiment. However, because of instrument failures, most parts of the SFB transport time series represent two ADCP subsets, as indicated in Table 1.

With more than three resources, the further gain in correlation is smaller, as three ADCPs already cover more than 90% of the total dense water transport with a spatial resolution close to the internal Rossby radius.

<sup>1</sup>RMS values represent standard deviation between the measured and actual transport for any single measurement. The error of the mean of an entire time series is smaller by a factor of  $1/\sqrt{n}$  with  $n$  as the number of independent observations.

## 4 Results of the field experiment

### 4.1 Hydrographic CTD profiles

The high variability of the overflow is reflected by hydrographic profiles obtained from various conductivity, temperature, and depth (CTD) casts taken during deployments at the mooring site B (Fig. 5, location marked as “B” in Fig. 1). The thickness of the overflow layer in the eight selected profiles at ADCP B varies between 100 (Poseidon P262 Station 237) and 500 m (Bjarni Sæmundsson 02/2002 Station 124). The density structure that is relevant for the overflow dynamics always shows distinct two-layer characteristics. In contrast, the sound speed profiles, primarily depending on temperature, lose their two-layer character when cold East Greenland Current water overlies the dense overflow. Nevertheless, during most of the deployment time warm AW was located above the overflow. The resulting contrast in sound speed allows to calculate the interface depth from PIES data, as will be shown later.

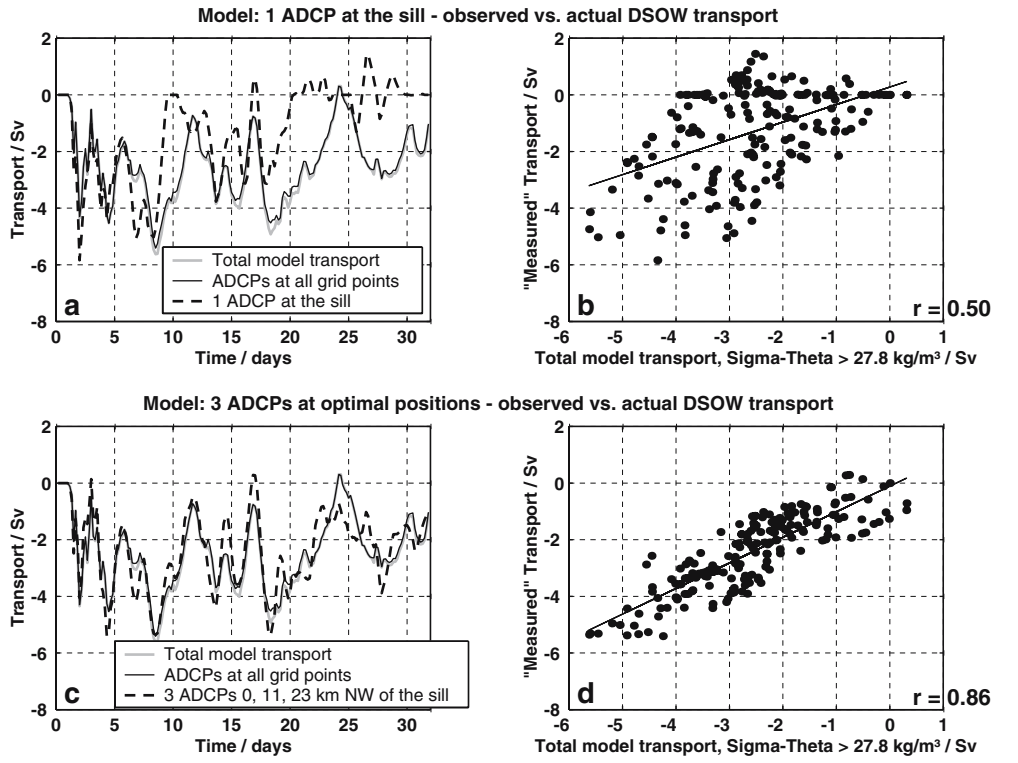
Close to the bottom ( $\sigma_\theta > 27.98 \text{ kg/m}^3$ ), variations of  $T/S$  properties (Fig. 5) are small compared to the strong contrasts in the diapycnal mixing region at the upper bound of the overflow ( $\sigma_\theta \leq 27.9 \text{ kg/m}^3$ ), which indicates mixing of different source water masses (e.g., Mauritzen 1996). Note intrusions of cold and fresh LAIW above the overflow at two stations (Fig. 5a and c, stations in 5/2001, 7/2002, and 8/2003), which are typical for mixing between the convergent parts of the East Greenland Current and AW contributions at the Iceland shelf break (Rudels et al. 2002).

### 4.2 Validation of acoustic observation methods

Three different, independent techniques were used in the field experiment to determine the upper DSOW interface depth: (1) depth of maximum current shear measured by the ADCP, (2) depth of maximum backscatter measured by the ADCP, (3) two-layer sound speed model for acoustic travel times and bottom pressure measured by PIES (discussed in previous section).

The upper DSOW boundary represents a distinct pycnocline (Fig. 5), which typically shows a large cross-strait slope (Fig. 1), which in turn leads to geostrophic current shear (Fig. 7).

**Fig. 4** Simulation of moorings in the model. Results with simulated ADCPs at all grid points (*thin line*) are almost identical to actual dense water transport in the model (*heavy line*). The *dashed line* indicates transports calculated from individual mooring array configurations. **a, b** (*upper panels*) An example for a configuration with one mooring directly at the sill. **c, d** (*lower panels*) The optimized configuration of three ADCPs, as deployed in August 2002



To identify the upper DSOW boundary from ADCP measurements, the maximum bin-to-bin velocity difference in the ADCP records is selected. Figures 6 and 7a,c show examples from the observations. This “maximum current

shear method” yields essentially similar results as the interface detection method Hansen et al. (2001) employed for the Faroe Bank Channel, where the velocity field also shows two-layer characteristics.

**Fig. 5** Hydrographic CTD profiles at location of ADCP B. Note the high vertical variability in the overflow layer thickness between different stations. Although density (b) always shows two clearly separated layers, the two-layer characteristics vanish in the temperature and sound speed profiles when warm Atlantic Water is present

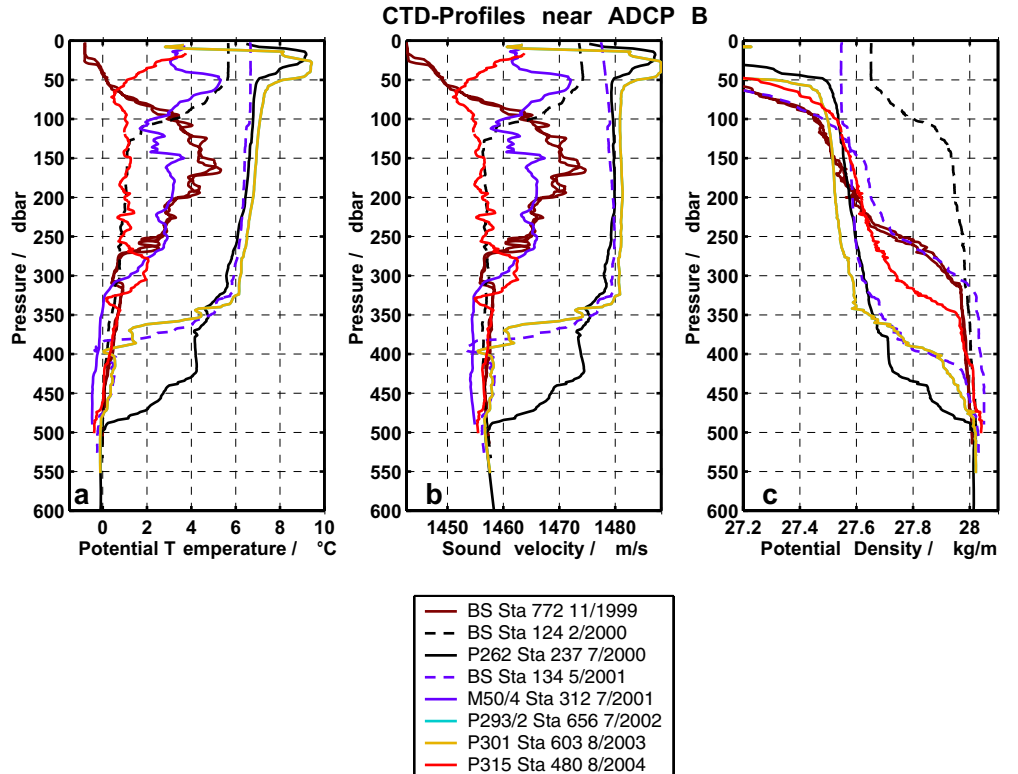
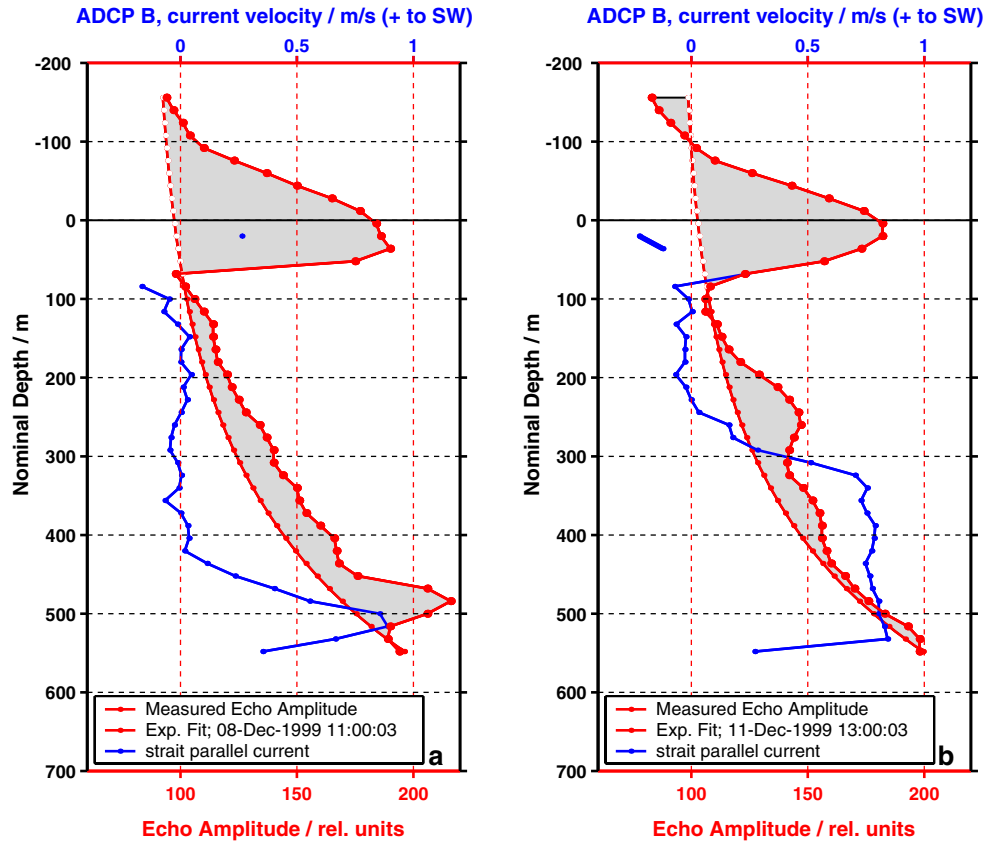


**Fig. 6** Two examples of backscatter profiles from ADCP B. In both panels, the *heavy line* denotes an individual observed profile of backscatter, whereas the *thin line* marks an empirical exponential fit of the theoretical clear-water backscatter (coefficients calculated from all bins below 100 m). The particle-associated backscatter is *shaded in gray*; it has maxima at 480 (a) and 250 m (b). Note that the large maximum above 80 m is caused by the surface reflection. Bins with negative nominal depths are included in the graphic to illustrate the shape of the entire surface echo. Additionally, the strait parallel current velocity is shown



Further, suspended matter (e.g., plankton) accumulates in the pycnocline, which leads to large backscatter amplitudes of the acoustic pings of the ADCP. Because idealized clear water backscatter decreases with distance from the bottom-mounted ADCP, particle-associated backscatter maxima can be identified as positive deviations from an empirical exponential fit of the theoretical clear water backscatter profile (see Fig. 6 for two examples). Most of the time, the “maximum backscatter method” agrees well with the maximum current shear method. However, its performance depends on plankton abundance. During periods with low productivity (winter) or diurnal vertical movements of plankton (Fig. 7d), the depth of maximum acoustic backscatter differs considerably from the maximum current shear. Thus, current shear, representing a dynamical criterion, may be considered as the most reliable method to determine the overflow plume thickness from ADCP data.

During the first deployment period (1999–2000), a PIES was moored just 500 m away from ADCP B. Here, the depth of maximum current shear and maximum backscatter (obtained from the ADCP data) can be compared with the interface depth calculated from PIES bottom pressure and acoustic travel time measurements (Fig. 8). The values are highly correlated and hence indicate the suitability of all three observation methods.

The data show the large short term variability the DSO is known for (e.g., Girton et al. 2001). The interface depth typically varies with amplitudes of  $O(100 \text{ m})$  and time

scales of 2–10 days, in agreement with Ross (1984). Estimates of the mean depth of the upper overflow plume interface are  $318 \pm 63 \text{ m}$  for method (1),  $311 \pm 67 \text{ m}$  for (2), and  $313 \pm 73 \text{ m}$  for (3), respectively. Further, the individual hydrographic profiles in Fig. 5 match well with the range established by the moored instrument data.

Vertical profiles of the current velocity (Fig. 9) also illustrate the two-layered structure of the cross-sill flow, with maximum current speeds reached in the overflow layer, that is driven by the density gradient between upstream and downstream regions of the Denmark Strait. The weaker, but significant outflow in the upper layer may be an indication of the additional barotropic wind stress forcing. Hence, the actual current velocity may be considered as a superposition of both forcing mechanisms (Kösters 2004). Both velocity and layer thickness show great variability. In contrast, the temporal mean (Fig. 9, heavy lines) appears more like a continuously stratified system, which cannot be used as an appropriate approximation for modeling the mean overflow transport. Hence, both plume thickness and velocity need to be observed to determine the actual dense water transport.

An equivalent plot for the model data is provided in Fig. 9b. The vertical structure of a bottom-intensified, barotropic outflow is similar in model and field data. The bottom frictional layer is less well represented in the model, which nevertheless does not affect the model’s

**Fig. 7** Example of time series of ADCP B in 1999: **a** Bin-to-bin velocity shear of strait parallel current (shaded). **b** Backscatter amplitude for the same period. The green line indicates the DSOW–AW interface depth determined by a PIES moored 500 m away from the ADCP. During a period of weak current shear (**c**), vertical diurnal movements of particle-associated backscatter are visible (**d**). Most likely, plankton moves to larger depths during daylight hours

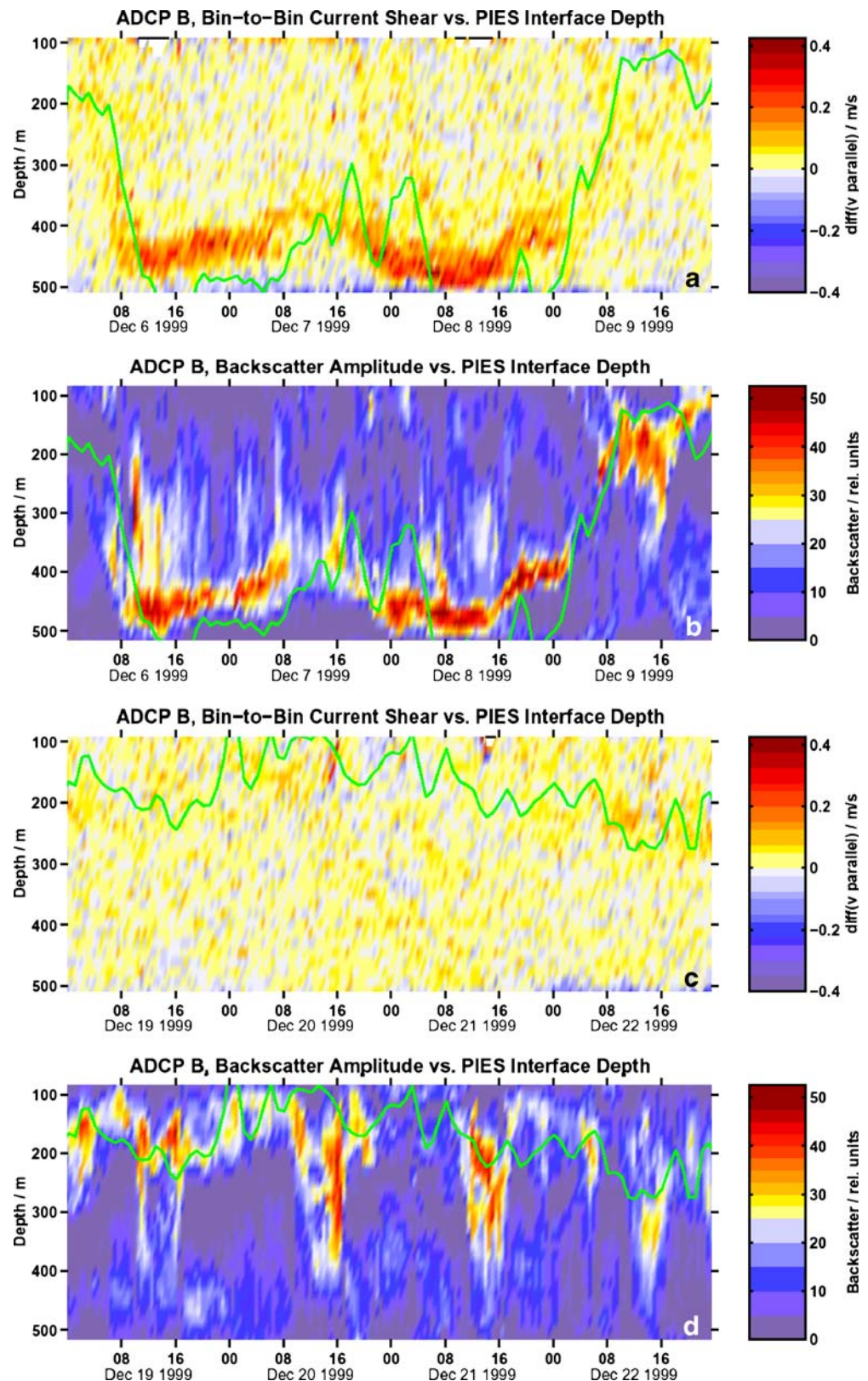
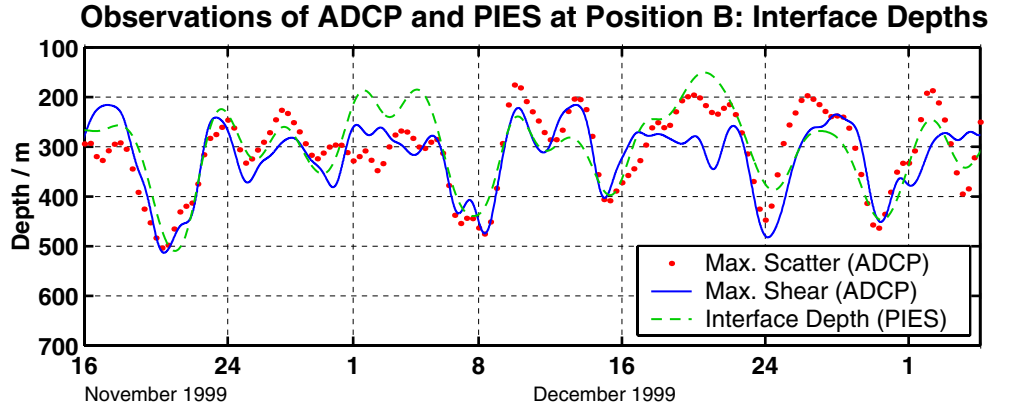


**Fig. 8** DSOW–AW interface depth, determined by three independent methods at the same position “B” in 1999–2000: ADCP: Maximum backscatter, maximum current shear, and PIES (two-layer model using observed vertical acoustic travel time and bottom pressure). During most of the time, all three methods agree within  $\pm 50$  m



performance to reproduce the dominant features of the overflow.

#### 4.3 Characteristics of the transport time series

Currently, time series are available from 1996 to 2005.

Here, the dynamic properties of the overflow for the time period 1999–2003 are examined, as only during this time was more than one instrument deployed, resolving the cross strait structure of the overflow.

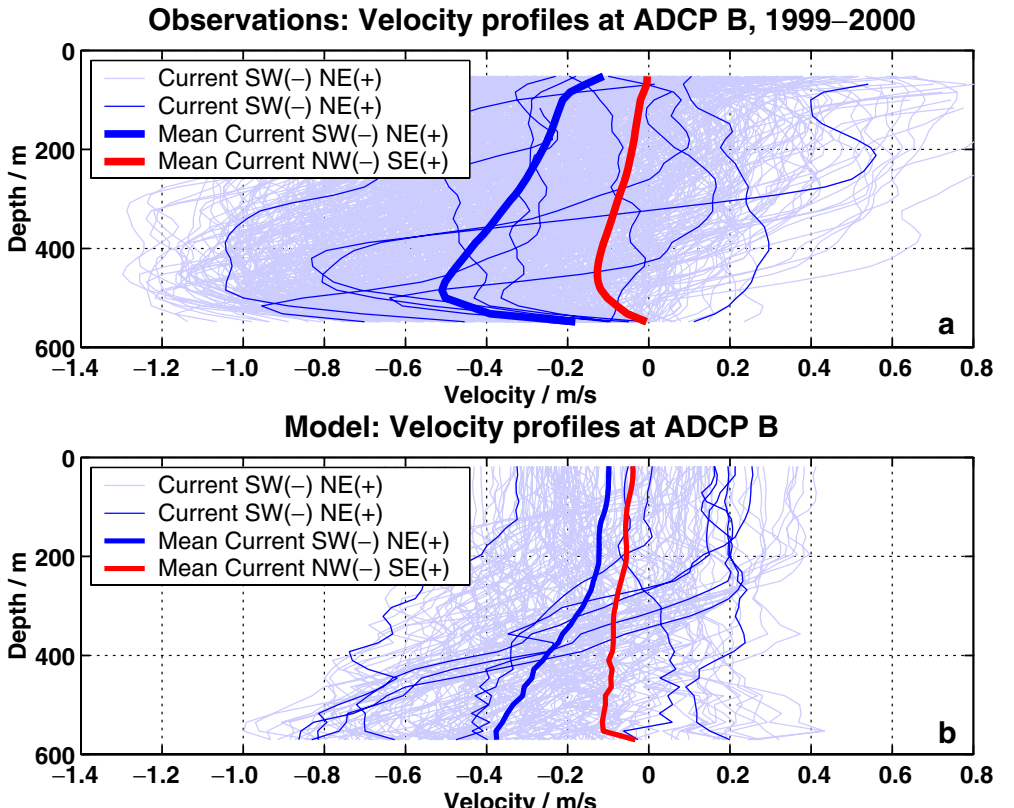
From Sept. 1999 to Feb. 2000, two ADCP moorings were deployed at the optimized positions of a two-mooring array (“A” and “B”, Fig. 1). From Jul. 2000 to summer 2003, the optimized three-mooring array (“A”,

“B” and “C”) was deployed. Unfortunately, because of mooring failure, data are available from only two locations, except for a short period of 3 months in 2002 with full coverage.

The velocity data were vertically integrated up to the interface depth defined by maximum current shear and multiplied by horizontal scale widths according to the optimization procedure (see Section 3.2). A remarkable interannual decrease from 3.7 (1999) to 3.1 Sv (2003) has been observed, which was addressed by Macrander et al. (2005). Here, the short term variability will be discussed in more detail.

The power spectral density of the overflow transport time series (Fig. 10) determined by autoregressive fits (Broersen 2002) has a broad peak around periods of 5 days,

**Fig. 9** **a** Observed current profiles at mooring position “B” (for location, see Fig. 1). Light lines indicate total range of variability, thin dark lines are arbitrarily selected individual profiles. Heavy lines show time averaged profiles. **b** Corresponding profiles in the model. Positive velocities are to the northeast, negative velocities represent outflow to the southwest



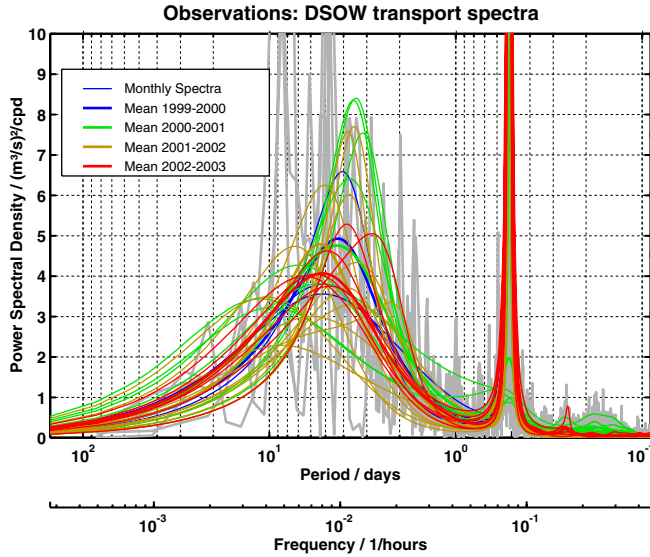


**Fig. 10** Power spectral density of DSOW transport from ADCP observations. Spectra were calculated using an autoregressive moving average model (Broersen 2002). Gray background lines depict actual monthly spectra to depict the observed variability. Maximum energy is associated with eddies on time scales of 2–10 days, and the  $M_2$  tide at 12 h 25 min

corresponding to the passage time scale of overflow eddies (Høyer and Quadfasel 2001; Käse et al. 2003) and confirms previous observations (e.g., Ross 1984, and others). The distinct narrow peak visible in the spectrum at a higher

frequency corresponds to the semidiurnal tide that modulates the outflow but has no significant net effect on the dense water transport (not shown).

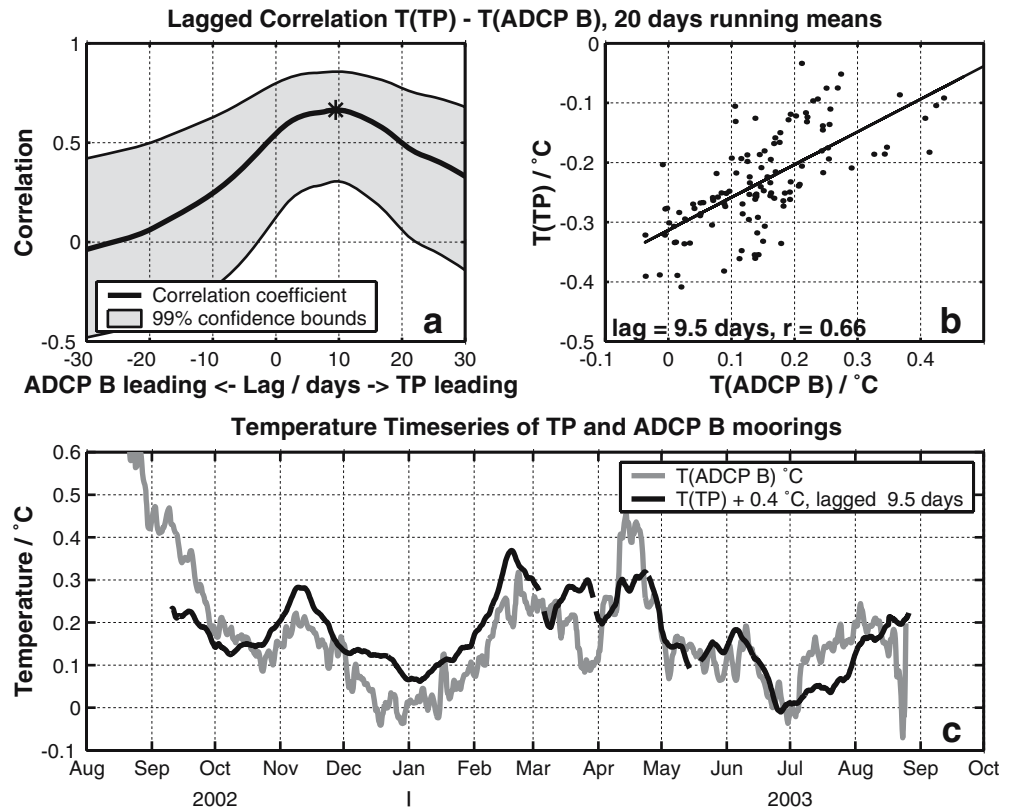
It is noteworthy that the total depth-integrated transport through the mooring array is in the same direction as the dense overflow. This is supported by velocity profiles (Fig. 9), indicating a mean current to the southwest at both ADCP A and B. The total volume transport through the observation array equals 5.7 Sv, with a fraction of 63% consisting of dense overflow water; the other 37% are lighter waters of the East Greenland Current and (to some extent) possibly recirculated AW.

The total barotropic flow through the Denmark Strait, however, may be different, as the mooring array has been optimized for dense water overflow observation and does not cover the shallower parts of the strait.

#### 4.4 Temperature variability and upstream pathways

All ADCP moorings at the sill were equipped with sensors to measure near-bottom temperature. The interannual temperature variability has been discussed by Macrander et al. (2005). Additionally, the temperature time series also allows upstream pathways of the overflow to be evaluated.

**Fig. 11** Lagged correlation of bottom temperature at TP mooring 93 km upstream of the sill and at ADCP B, 20 days running means. **a** Correlation as function of time lag, showing a maximum for a time lag of 9.5 days, which corresponds to a temperature anomaly propagation speed of 0.11 m/s from the TP site to the sill. 99% confidence bounds shaded in background. **b** Scatter plot for correlation maximum. **c** Time series of temperature. Note that the ADCP B temperature records are shifted by  $0.4^{\circ}\text{C}$  to match the colder upstream values at TP



#### 4.4.1 Advection of water masses to the sill

In 2002–2003, a mooring equipped with temperature sensors called “TP” was deployed at the Iceland shelf edge 93 km northeast of the sill to monitor the upstream reservoir conditions. The temperature records of the deepest sensor are significantly correlated with the temperature data at ADCP B (Fig. 11). This high correlation supports the findings of Jónsson and Valdimarsson (2004a,b) that a major part of the overflow originates from the Iceland side of the strait rather than from the Greenland side (Jónsson 1999). Temperatures at the sill are around 0.4°C higher, although, suggesting that on the way to the sill, this water may have been mixed with warmer AW (Jónsson and Valdimarsson 2004a,b) but not with the colder waters of the East Greenland Current.

For 20 days running mean time series, a significant correlation maximum of 0.66 at a time lag of 9.5 days between the TP mooring and ADCP B (Fig. 11) is found. This corresponds to a mean advection velocity of 0.11 m/s for temperature anomalies from the TP site 93 km northeast of the sill, essentially similar to the mean speed of 0.096 m/s observed by Jónsson (1999) and Jónsson and Valdimarsson (2004a,b) at the IS7 mooring site on the Iceland shelf edge 200 km upstream of the sill (see insert map in Fig. 1). The continuation of this flow towards the sill is additionally supported by expendable current profiler measurements (Girton and Sanford 2003).

Repeated Icelandic hydrographic data at the Kögur 5 (KG5) station close to the IS7 site do not show the interannual warming signal that was observed at the sill. A closer look at the time series at the sill reveals that water masses of different temperature pass the ADCP B mooring. Although the coldest waters at the sill have a similar temperature to those passing KG5, water masses up to 1°C warmer also contribute to the overflow. Sudden temperature shifts suggest that the different source water masses are not yet well mixed at the sill. Hence, changes of the mean temperature of the overflow primarily depend on the relative contribution of different source water masses rather than changing properties of individual source water masses in the Nordic Seas.

The water mass properties at the sill will be studied in more detail, when the first moored MicroCat (measuring temperature and salinity) that was deployed in 2005 will be recovered in autumn 2006.

#### 4.4.2 Communication by waves

In theory, it may be expected that reservoir height changes at the TP site are also communicated to the sill by long gravity waves at the interface. With appropriate parameter settings for the Denmark Strait ( $\Delta\rho = 0.48 \text{ kgm}^{-3}$ , upper and lower layer thicknesses  $H_1 = 240 \text{ m}$  and  $H_2 = 360 \text{ m}$ ), a phase velocity of  $c = \sqrt{g'(H_2 H_1)/(H_2 + H_1)} = 0.81 \text{ ms}^{-1}$  is found.

As in a continuously stratified system, height changes of isopycnals and isotherms are associated with temperature changes at a fixed depth, this fast communication might show up as a lagged correlation between TP and sill temperature records. In fact, a weak but statistically significant correlation maximum of  $r = 0.19$  has been found in the data (not shown). The time lag of 31 h corresponds to a propagation speed of  $0.83 \text{ ms}^{-1}$ . Thus, the observed lagged correlation is possibly a (weak) indication of communication between the upstream basin and the sill on faster-than-advection time scales.

#### 4.5 Geostrophic estimates

In the high-resolution process model, > 90% of the overflow transport at the sill is geostrophically balanced (Fig. 2). Here, PIES observations are investigated to test whether geostrophy is a valid approximation of the real overflow. Because of instrument losses, two PIES were available only during the period from July 2000 to May 2001. These instruments were located on both sides of ADCP B, with a distance of 13 km between the two PIES. As the spacial extent of the PIES array is on the order of just one internal Rossby radius, the ADCP B current observations are representative for the mean flow between both PIES and may be compared with the geostrophic estimates.

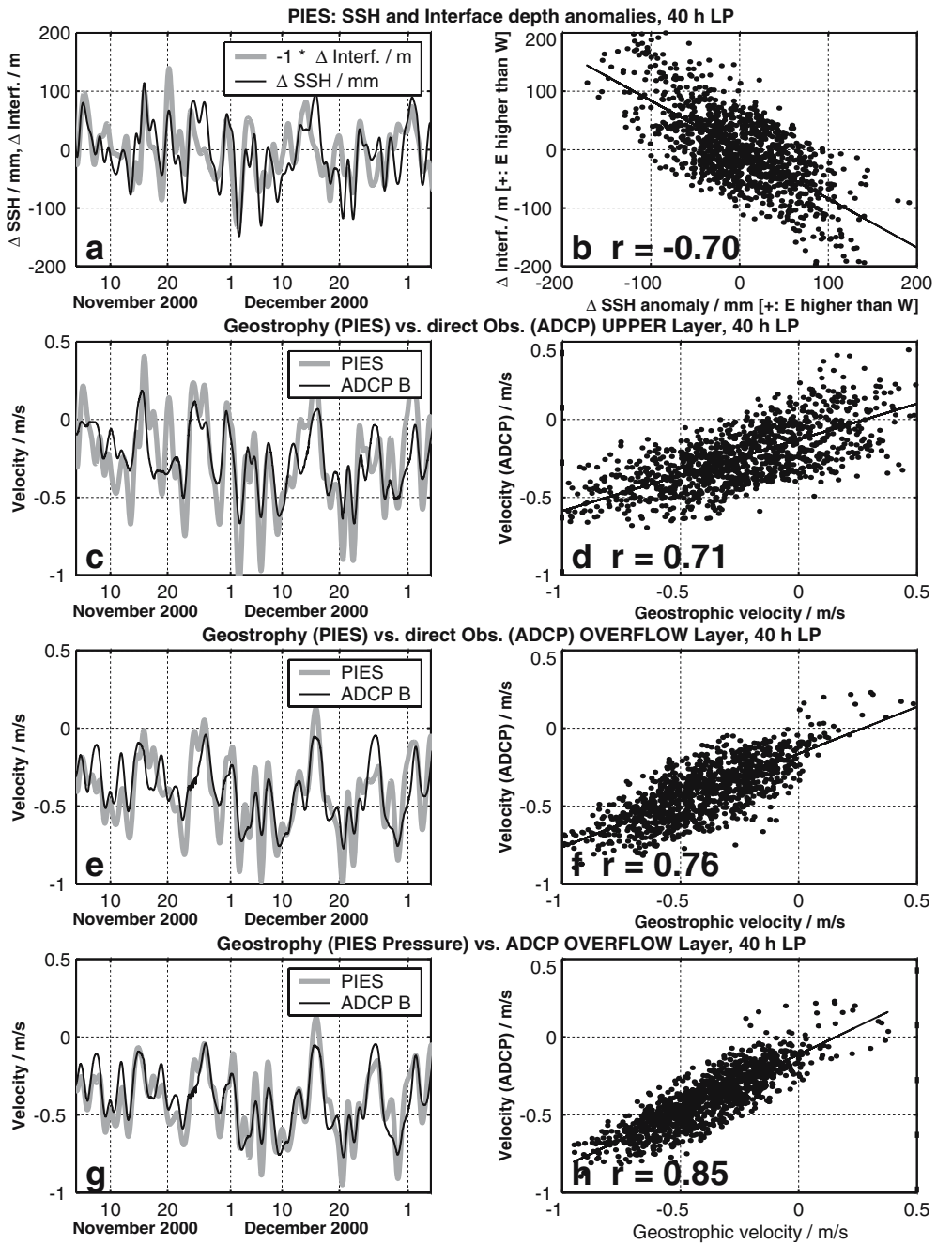
Upper and lower layer velocities were calculated by Eqs. 3 and 4. As the absolute SSH (observed by PIES) relative to the geoid is unknown, only SSH slope anomalies can be derived from a two-PIES array. Absolute geostrophic velocities were obtained by referencing the mean geostrophic surface current to the mean surface velocity measured by ADCP B, which was moored between both PIES. Additionally, geostrophic velocities of the overflow layer were also derived from pressure anomalies measured by the PIES.

In the observations, the direct ADCP measurements compare well with the geostrophic estimates both in phase and amplitude of variability (Fig. 12). For the overflow layer, geostrophic velocity obtained from the PIES pressure records and ADCP data are correlated with  $r = 0.85$ . The two-layer SSH and interface slope still yields a correlation of 0.76 and 0.71 for the overflow and surface layers, respectively. Although on shorter time scales, some ageostrophic components are evident; the low-passed PIES measurements show that the DSO at the sill can be approximated by a geostrophic two-layer system.

Thus, for long-term overflow variability monitoring, SSH and interface depth estimates obtained from PIES may allow realistic estimates. Nevertheless, some direct velocity observations (e.g., ship sections with vessel-mounted ADCP) are necessary to determine the time-independent offset for referencing the geostrophic current anomalies to absolute velocities.

Interestingly, the observed time series of SSH and interface depth difference anomalies between the two PIES are anticorrelated (Fig. 12a,b); on longer time scales (>20

**Fig. 12** Evidence for geostrophic balance in the observations. Left panels show a typical example of the 40-h-low passed time series 2000–2001, whereas the right-hand panels show corresponding scatter plots, linear fits, and correlation coefficients. **a, b** Anticorrelation of cross-current SSH slope and upper DSOW boundary, measured between two PIES with a distance of 13 km. Note the different scaling (millimeters for SSH and meters for interface slope). In **a**, the interface slope is shown with reverse sign to better illustrate the correlation with SSH. **c, d** Geostrophic velocities obtained from PIES SSH measurements (gray) and actual current velocities observed by ADCP B (thin black line; vertical average above layer of maximum current shear). **e, f** Geostrophic velocities obtained from PIES SSH and Interface depth measurements (gray) and direct observation of ADCP B (thin black line) for the overflow layer (vertical average). **g, h** Same as above, but geostrophic estimates directly derived from the PIES pressure records. All currents shown represent the velocity component normal to the PIES section line, with positive values to the northeast



days), the correlation is even larger than 0.95. This anticorrelation implies that the cross-strait slope of the DSOW plume interface could be inferred from SSH measurements alone, which may open a perspective of overflow monitoring by satellite altimetry.

First comparisons of Topex/Poseidon alongtrack altimetry (Berwin 2003a,b) and ADCP surface current velocity revealed, that satellites in fact can capture geostrophic surface velocity (not shown). However, estimates of the dense overflow transport failed to reproduce the observed variability; in particular, the interannual decrease was not found in the satellite-derived estimates. Probably, the combination of low sampling rate (once in 3 days), aliasing of short-term variability, noise in the satellite SSH data, and

the not-perfect anticorrelation of SSH and DSOW interface slope downgrades the inferred overflow transport. Further, only a correlation of SSH and DSOW interface slope was found in the PIES time series; overall changes of the reservoir height or plume thickness appear to have no surface signature at the sill.

Nevertheless, altimetry may prove useful to monitor the wind-driven barotropic flow through the Denmark Strait. It remains to future investigations to determine if long-term DSO transport time series can be obtained by the combination of alongtrack altimetry for the barotropic flow and upstream reservoir height data for the density driven part of the overflow.

## 5 Discussion and future prospects

The SFB project showed that acoustic instruments such as ADCPs and PIES are appropriate to determine the flow through sea straits with different water masses separated by distinct density fronts. If sound velocity is different between the water masses (as is the case for AW and DSOW in the Denmark Strait), PIES can be used not only for SSH but also for interface depth estimates. The use of a high-resolution process model (grid scale three times smaller than the internal Rossby radius) proved valuable for evaluating an optimized mooring array and for determining reliable error estimates for individual mooring configurations.

The observations confirmed that the DSO at the sill is predominantly in geostrophic balance, which allows the use of PIES for integrating transport measurements. For long-term monitoring of the dense overflow with respect to climate change, both the upstream reservoir height and the wind-driven barotropic transport should be observed.

**Acknowledgments** This work was carried out at IFM-GEOMAR Kiel, Germany, in SFB 460 funded by the Deutsche Forschungsgemeinschaft, and at the Marine Research Institute Reykjavík, Iceland. We thank the crews of the research vessels “Árni Friðriksson,” “Bjarni Sæmundsson,” “Meteor,” and “Poseidon” for their invaluable support in the field experiment. We acknowledge the helpful comments of two anonymous reviewers, which significantly improved this manuscript.

## 1 Appendix: Error estimates

### – Direct observations: ADCP

For ADCP observations, errors in current velocity and detection of backscatter or current shear maxima yield a transport error of 0.13 Sv for each single measurement. However, these instrumental errors are smaller than those caused by natural variability and biases because of the chosen deployment positions (discussed in Section 3.2). In the field experiment, the model-derived systematic underestimate and the RMS errors of any single transport estimate are specified in Table 1. For approximately 300 days of each observation period and an integral time scale of 4 days, this results in 75 independent estimates. Hence, the error of the mean transport is subsequently reduced by a factor of  $\sqrt{75} \approx 8.7$  to the order 0.1 Sv.

### – Geostrophy: PIES

Uncertainties in travel time and bottom-pressure measurements cause errors in the interface and SSH estimates and corresponding two-layer geostrophic transport values. For any single measurement, a transport error of 0.12 Sv is caused by an interface depth RMS error of 12 m for each PIES (40-h low-passed values); 0.45 Sv results from SSH slope RMS errors of 9 mm. Nevertheless, the geostrophic estimates have to be corrected by a constant offset derived from independent current velocity observations, as PIES

does not determine the absolute SSH slope relative to the geoid.

## References

- Aagaard K, Malmberg S-A (1978) Low frequency characteristics of the Denmark Strait overflow. ICES, CM 1978/C:47
- Bacon S (1998) Decadal variability in the outflow from the Nordic Seas to the deep Atlantic Ocean. *Nature* 394:871–874
- Berwin R (2003a) TOPEX/POSEIDON sea surface height anomaly product user’s reference manual, version 2
- Berwin R (2003b) Jason-1 sea surface height anomaly product user’s reference manual, version 2
- Biastoch A, Käse RH, Stammer DB (2003) The sensitivity of the Greenland–Scotland overflow to forcing changes. *J Phys Oceanogr* 33:2307–2319
- Borenäs K, Lundberg P (1986) Rotating hydraulics of flow in a parabolic channel. *J Fluid Mech* 167:309–326
- Broersen PMT (2002) Automatic spectral analysis with time series models. *IEEE Trans Instrum Meas* 51(2):211–216
- Dickson RR, Brown J (1994) The production of North Atlantic deep water: sources, rates and pathways. *J Geophys Res* 99:12319–12341
- Dickson RR, Lazier J, Meincke J, Rhines P, Swift J (1996) Long-term coordinated changes in the convective activity of the North Atlantic. *Prog Oceanogr* 38:241–295
- Dickson B, Meincke J, Vassie I, Jungclaus J, Østerhus S (1999) Possible predictability in overflow from the Denmark Strait. *Nature* 397:243–246
- Dietrich G, Kalle K, Krauß W, Siedler G (1975) Allgemeine meereskunde, 3rd edn. Bornträger-Verlag, Berlin, Stuttgart
- Fofonoff NP (1985) Physical properties of seawater. *J Geophys Res* 90:3332–3342
- Gill AE (1977) The hydraulics of rotating-channel flow. *J Fluid Mech* 80:641–671
- Girton JB (2001) Dynamics of transport and variability in the Denmark Strait overflow. Ph.D. thesis, University of Washington, Seattle
- Girton JB, Sanford TB (2003) Descent and modification of the overflow plume in the Denmark Strait. *J Phys Oceanogr* 33(7):1351–1364
- Girton JB, Sanford TB, Käse RH (2001) Synoptics of the Denmark Strait overflow. *Geophys Res Lett* 28:1619–1622
- Hansen B, Østerhus S (2000) North Atlantic–Nordic Seas exchanges. *Prog Oceanogr* 45:109–208
- Hansen B, Turrell WR, Østerhus S (2001) Decreasing overflow from the Nordic Seas into the Atlantic Ocean through the Faroe Bank channel since 1950. *Nature* 411:927–930. DOI [10.1038/35082034](https://doi.org/10.1038/35082034)
- Hoyer JL, Quadfasel D (2001) Detection of deep overflows with satellite altimetry. *Geophys Res Lett* 28(8):1611
- Jónsson S (1999) The circulation in the northern part of the Denmark Strait and its variability. ICES CM, L:06, 9 pp
- Jónsson S, Valdimarsson H (2004a) A new path for the Denmark Strait overflow water from the Iceland Sea to Denmark Strait. *Geophys Res Lett* 31:L03305, DOI [10.1029/2003GL019214](https://doi.org/10.1029/2003GL019214)
- Jónsson S, Valdimarsson H (2004b) An ocean current over the continental slope northwest of Iceland carrying Denmark Strait overflow water from the Iceland Sea to Denmark Strait. ICES CM, 2004/N:04, 11 pp
- Käse RH (2006) A Riccati model for Denmark Strait overflow variability. *Geophys Res Lett* 33:L21S09. DOI [10.1029/2006GL026915](https://doi.org/10.1029/2006GL026915)
- Käse RH, Oschlies A (2000) Flow through Denmark Strait. *J Geophys Res* 105(28):527–528, 546
- Käse RH, Girton JB, Sanford TB (2003) Structure and variability of the Denmark Strait overflow: model and observations. *J Geophys Res* 108(C6):3181
- Killworth PD, McDonald NR (1993) Maximal reduced-gravity flux in rotating hydraulics. *Deep-sea Res I*(42):859–871

- Kösters F (2004) Denmark Strait overflow: comparing model results and hydraulic transport estimates. *J Geophys Res* 109:C10011, DOI [10.1029/2004JC002297](https://doi.org/10.1029/2004JC002297)
- Macrander A, Send U, Valdimarsson H, Jónsson S, Käse RH (2005) Interannual changes in the overflow from the Nordic Seas into the Atlantic Ocean through Denmark Strait. *Geophys Res Lett* 32:L06606, DOI [10.1029/2004GL021463](https://doi.org/10.1029/2004GL021463)
- Mauritzen C (1996) Production of dense overflow waters feeding the North Atlantic across the Greenland–Scotland ridge: Part I. Evidence for a revised circulation scheme. *Deep-sea Res* 43:769–806
- McCartney M, Donohue K, Curry R, Mauritzen C, Bacon S (1998) Did the overflow from the Nordic Seas intensify in 1996–1997? *Int WOCE Newsl* 31:3–7
- Meinen CS, Watts DR (1998) Calibrating inverted echo sounders equipped with pressure sensors. *J Atmos Ocean Technol* 15(6):1339–1345
- Nikolopoulos A, Borenäs K, Hietala R, Lundberg P (2003) Hydraulic estimates of Denmark Strait overflow. *J Geophys Res* 108(C3)
- Ross CK (1984) Temperature–salinity characteristics of the “overflow” water in Denmark Strait during “OVERFLOW ’73”. *Rapp P-v Réun Cons Int Explor Mer* 185:111–119
- Rudels B, Fahrbach E, Meincke J, Budéus G, Eriksson P (2002) The East Greenland current and its contribution to the Denmark Strait overflow. *ICES J Mar Sci* 59:1133–1154
- Saunders PM (2001) The dense northern overflows. In: Siedler G (ed) *Ocean circulation and climate*. Int Geophys Ser (San Diego) 77:401–418
- Swift JH (1986) The arctic waters. In: Hurdle BG (ed) *The Nordic Seas*. Springer, Berlin Heidelberg New York, pp 124–153
- Whitehead JA (1998) Topographic control of oceanic flows in deep passages. *Rev Geophys* 36(3):423–440
- Worthington LV (1969) An attempt to measure the volume transport of Norwegian Sea overflow water through the Denmark Strait. *Deep-sea Res* 16:421–432